Appl Nanosci (2012) 2:305–310
DOI 10.1007/s13204-012-0114-8

ORIGINAL ARTICLE

Effect of Y-doping on optical properties of multiferroics $BiFeO_3$ nanoparticles

A. Mukherjee · Sk. M. Hossain · M. Pal · S. Basu

Received: 9 November 2011 / Accepted: 30 March 2012 / Published online: 5 May 2012

Abstract We have synthesized yttrium-doped bismuth ferrite nanoparticles through a modified Pechini technique. X-ray diffractometer, transmission electron microscope (TEM) and ultraviolet–visible spectrophotometer (UV–Vis) probes have been utilized to characterize the nanoparticles. Average particle size estimated from TEM found to be 29 nm for $Bi_{0.99}Y_{0.01}FeO_3$ samples. The band gap of the prepared BFO and BYFO nanoparticles varies from 1.97 to 2.29 eV, that is, within the visible range of the sunlight. This property of these nanoparticles can be utilized in photo catalytic decomposition of organic contaminants, such as Rhodamine-B (RhB) under visible light irradiation. We have explored and observed that RhB degrade up to 8 % while mixed with $Bi_{0.90}Y_{0.1}FeO_3$ for 1 h under 40 W lamp due to photo catalysis together with sensitization.

Keywords Multiferroics · Y-doped $BiFeO_3$ nanoparticles · Band gap · Photo catalyst

Introduction

Multiferroics, materials that show simultaneous existence of two or more ferroic order and can be switched hysterically by the application of one another are the recent interest in the field of modern research. Multiferroic materials show a strong magnetoelectric coupling over a certain range of temperature (Fiebig 2005; Eerenstein et al. 2006; Cheong and Mostovoy 2007; Ramesh and Spaldin 2007). These materials can be widely used in the field of spintronics, electromagnetic shielding, storage devices, transducers, etc. Among the various multiferroic materials, $BiFeO_3$ (BFO) shows simultaneous existence of ferroelectricity with a high Curie temperature of ($T \sim 830$ °C) and a G-type anti-ferromagnetism with a Neel temperature of ($T \sim 370$ °C), which makes it possible to show magneto electric coupling above room temperature. It has a long-range cycloidal spin arrangement of wavelength 62 nm incommensurate within the lattice.

However, beside these potential applications of BFO, there are some serious problems, such as high leakage current arising from impurities, defects or non-stoichiometry (Wang et al. 2004; Park et al. 2007). Its remnant magnetization (M_r) and potential magnetoelectric effect both vanish on a macroscopic scale, giving rise to a quadratic ferromagnetoelectric behavior rather than a linear ferromagnetoelectric behavior (Fiebig 2005; Eerenstein et al. 2006). To improve the electrical properties of the BFO, several research groups have attempted to dope with +3 valence lanthanide ions [La^{3+}, Nd^{3+} or Sm^{3+}] at the A site of BFO (ABO_3) (Zhang et al. 2006; Yuan et al. 2006; Singh et al. 2006). It is possible to destroy the spin cycloid and hence to release the non-zero macroscopic M_r and potential magnetoelectric effect. It has been demonstrated that A site substituted BFO multiferroics accompany their non-zero macroscopic M_r with destroyed spin cycloids (Wang et al. 2005, 2006; Lee et al. 2005; Eerenstein et al. 2005).

It also shows some interesting optical properties, which can be used to design many optical devices such as photo

A. Mukherjee · Sk. M. Hossain · S. Basu (✉)
Department of Physics, National Institute of Technology, Durgapur 713209, India
e-mail: sou_menbasu@yahoo.com

M. Pal
CSIR-Central Mechanical Engineering Research Institute, Durgapur 713209, India

catalyst. As BFO has small band gap, it can be used as a visible light photo catalyst for water splitting and degradation of organic contaminant. H_2 can be produced under visible light irradiation in $SrTiO_3$-coated BFO core/shell nanostructures (Lou and Maggard 2006). BFO nanoparticles are good photo catalyst for the degradation of methyl orange (Gao et al. 2007). It has been reported earlier that BFO plates possesses higher photo catalytic activity than that of bulk BFO for photodecolorization of orange II (Lu et al. 2007). Beside these important applications, its photo catalytic ability degrades due to the presence of impurity phases and structural instability. However, Luo et al. (2010) showed that BFO–H_2O_2 system has enhanced photo catalytic activity and can be used as a Fenton-like catalyst. Rare earth doping on the A or B site of the ABO_3 lattice has played an important role in altering its many properties. Structural transformation from rhombohedral to orthorhombic or tetrahedral change the electronic or crystal structure of BFO which may enhance its photo catalytic activity. In this article, we have reported the synthesis of rare earth yttrium-doped $BiFeO_3$ (BYFO) nanoparticles by modified Pechini method and studied their structural and optical properties, which is very much necessary for design of optical instruments. The ionic radius of Y^{+3} (1.04 Å) is smaller than that of Bi^{+3} (1.17 Å), which resulted in large lattice distortion and enhance its optical applications.

Experimental

Yttrium-doped $BiFeO_3$ (BFO/BYFO) ($Bi_{1-x}Y_xFeO_3$ with $x = 0, 0.01, 0.05, 0.10$) nanoparticles were prepared by a modified Pechini method (Pechini et al. 1967) using metal nitrates as precursors. Initially calculated amount Bi $(NO_3)_3{\cdot}5H_2O$ and Y $(NO_3)_3{\cdot}10H_2O$ with total 0.015 mole were mixed in 10 ml distilled water under continuous stirring. In another beaker, 0.015 mole of Fe $(NO_3)_3{\cdot}9H_2O$ was mixed in 10 ml distilled water under continuous stirring. The two solutions were mixed after stirring for 2 h followed by continuous ultrasonication for 2 h. HNO_3 was used to maintain the PH of the solution to 2. In the second step, maleic acid (0.03 mol) was dissolved in distilled water (30 ml) in a separate beaker. Metal nitrate precursor solutions were added to the maleic acid solution under constant ultrasonication. Polyethylene glycol (PEG) in a molar ratio to maleic acid of 1:1 was finally added to the solution as a polymerizing agent and undergoes continuous ultrasonication for 3 h. The solution was then evaporated to dry polyester precursor powder in a hot-air oven. Finally, the grinded precursor powders were calcined in air at 600 °C for 2 h with a heating rate of 400 °C h^{-1}.

Characterization

X-ray diffraction (XRD) spectra of these samples were recorded with an X Pert Pro X-ray diffractometer (PANLYTICAL, Almelo, The Netherlands) with nickel-filtered Cu-K_α radiation ($\lambda = 1.5414$ Å) in 2θ range from 20° to 80°. Electron microscopy was used to study the morphology of the $Bi_{1-x}Y_xFeO_3$. A very small part of the samples were dispersed in an ethyl alcohol solution, and one drop of dispersed solution was cast on a carbon-coated copper grid to obtain the TEM images. TEM was performed on a JEOL 2010 operated at 200 kV. Fourier transform infrared spectroscopy (FTIR), ultraviolet–visible (UV–Vis), and photoluminescence (PL) spectroscopy were used to characterize the specimens. Ultraviolet–visible (UV–Vis) spectroscopy was performed on a double-beam spectrophotometer (Hitachi, U-3010, Waltham, MA) using ethyl alcohol as a solvent. Photoluminescence (PL) spectroscopy was performed on a Hitachi fluorescence spectrophotometer (F-2500). Fourier transform infrared spectroscopy (FTIR) was recorded on a Nicolet NEXUS FTIR spectrometer (Vernon Hills, IL) within a range of 450–4,000 cm^{-1} using KBr powder. The photo catalytic activity was performed by the degradation of Rhodamine-B (RhB) in aqueous solution in dark and under visible light irradiation using a 40 W lamp. The reaction was performed at room temperature with 10 ml RhB (5 mg l^{-1}) solution, adjusted to a fixed pH value with 1 drop of HCl and 10 mg of the photo catalyst ($Bi_{0.90}Y_{0.1}FeO_3$). The photo catalytic activity was measured from the absorbance at 542 nm using a UV−Vis spectrophotometer.

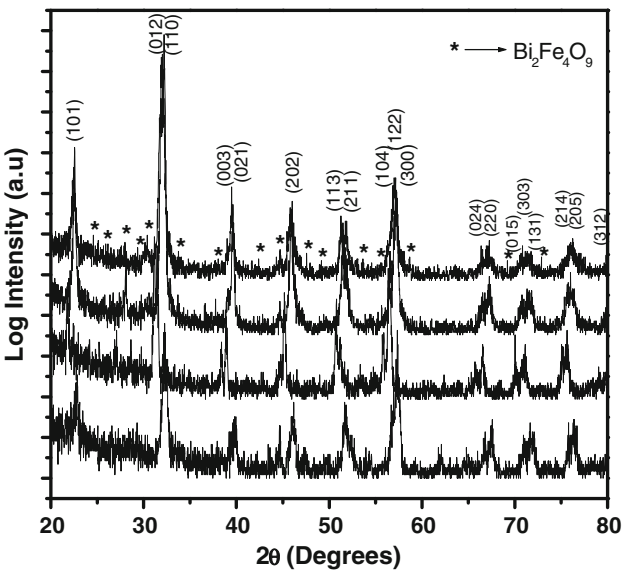

Fig. 1 XRD of samples prepared at 600 °C **a** $BiFeO_3$, **b** $Bi_{0.99}Y_{0.01}FeO_3$, **c** $Bi_{0.95}Y_{0.05}FeO_3$ and **d** $Bi_{0.90}Y_{0.10}FeO_3$

Results and discussion

XRD patterns of the samples calcined at 600 °C with different concentration of Yttrium are shown in Fig. 1. Here we have plotted the intensity in logarithmic scale so that low intensity peaks will shoot-up and can be easily able to judge the single phase nature of the samples. All the prominent peaks in XRD pattern are indexed to various (hkl) planes of BFO (JCPDS No. 00-014-0181), indicating the formation of BFO and BYFO. It has been found that BFO is almost single phase; however, a second phase $Bi_2Fe_4O_9$ appears (JCPDS No. 01-074-1098), which is almost removed when 10 % doping concentration is attained.

Figure 2a shows TEM image of the $Bi_{0.99}Y_{0.01}FeO_3$ sample. The particle size distribution is presented in Fig. 2b. The mean value of particle size estimated as 29 nm with standard deviation 1.6 nm by fitting the experimental data obtained from TEM picture with log-normal distribution function. A high-resolution TEM image from a portion of the $Bi_{0.99}Y_{0.01}FeO_3$ nanoparticle is shown in Fig. 2c. Clear lattice fringes are visible suggesting the samples are defect free and highly crystalline in nature. The observed lattice spacing is measured to be 3.9 and 2.9 Å which corresponds to (101) and (012) lattice planes of rhombohedral BFO. Figure 2d shows the SAED pattern taken from Fig. 2a the sharp diffraction spots confirmed the well developed, polycrystalline nature of

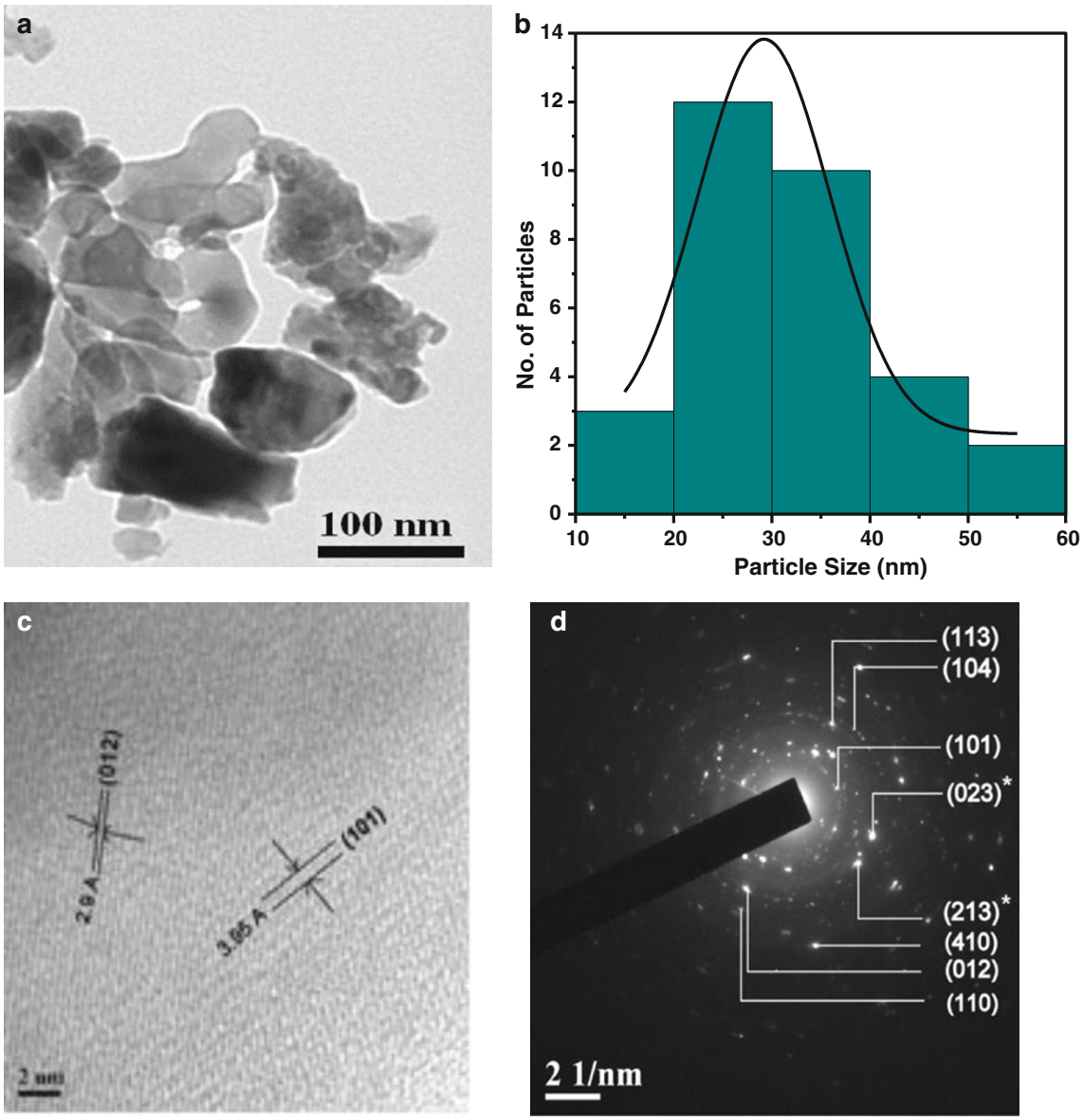

Fig. 2 **a** A typical TEM image of the $Bi_{0.99}Y_{0.01}FeO_3$. The particle size distribution is presented in **b**. **c** The high-resolution TEM image of $Bi_{0.99}Y_{0.01}FeO_3$ samples taken from a portion of **a**. **d** The SAED pattern taken from **a**

BFO nanoparticles. However, the planes (023)* and (213)* matches with $Bi_2Fe_4O_9$ (JCPDS No. 01-074-1098).

Figure 3 shows the FTIR spectra of BFO and BYFO. The fundamental absorptions are observed in the wavelength region 450−550 cm^{-1}. This band is attributed to the bending vibration of the Fe−O bond in the FeO_6 octahedral unit (Rao et al. 1970) and also due to the BiO_6 octahedral structure unit (Som et al. 1992). The broad band at 3,000–3,600 cm^{-1} arose from the anti-symmetric and symmetric stretching of bond H_2O and OH^{-1} groups, while a band at 1,700 cm^{-1} corresponded to the bending vibrations of H_2O (Slamovich et al. 1996; Li et al. 1989). The band at around 1,390 cm^{-1} was due to the presence of trapped nitrates (Nakagawa and Walter 1969). The bands around 1,300 cm^{-1} possibly correspond to the formation of esters during the condensation reaction between ethylene glycol and maleic acid in the sol-formation process. Evidence of carbonate groups, as signified by the band at 1,500–1,300 cm^{-1}, as well as at peaks at 1,120–1,070 cm^{-1} and 850 cm^{-1} (Zhang et al. 2006). No significant shift is observed in peak shifting due to yttrium doping.

Figure 4 shows the UV−Vis absorption spectra of different samples. The UV–Vis absorption peaks for $BiFeO_3$, $Bi_{0.99}Y_{0.01}FeO_3$, $Bi_{0.95}Y_{0.05}FeO_3$, and $Bi_{0.90}Y_{0.10}FeO_3$ are seen at 571, 518, 485, and 469 nm, respectively. These indicate a change in the electronic structure of $BiFeO_3$ with increase in the dopant concentration. However, as we move to higher dopant concentration, a significant shift of 100 nm towards the shorter wavelength side is observed, which might be due to the creation of oxygen vacancy (Roy et al. 2007). These indicate an obvious blue shift when $BiFeO_3$ is doped with yttrium and thus an increased band gap. The band gap for the prepared samples has been calculated from the point of maximum change in the

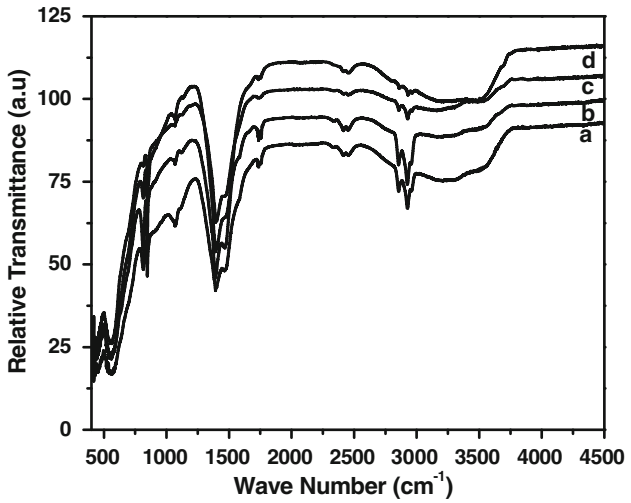

Fig. 3 FTIR spectra of **a** $BiFeO_3$, **b** $Bi_{0.99}Y_{0.01}FeO_3$, **c** $Bi_{0.95}Y_{0.05}FeO_3$ and **d** $Bi_{0.90}Y_{0.10}FeO_3$

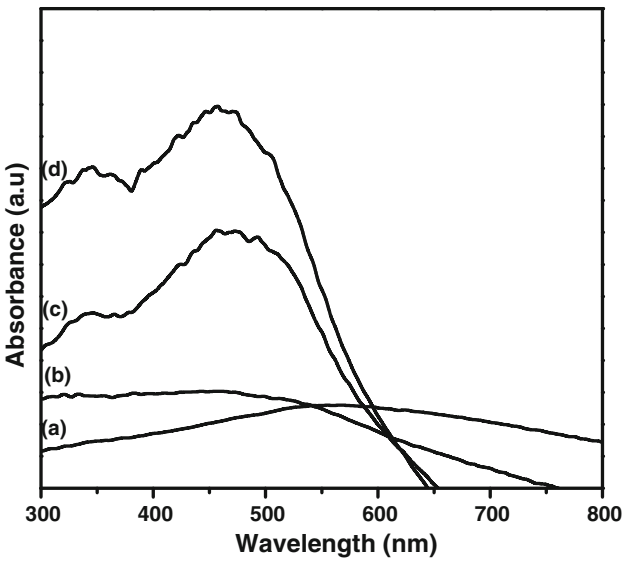

Fig. 4 Absorption spectra of **a** $BiFeO_3$, **b** $Bi_{0.99}Y_{0.01}FeO_3$, **c** $Bi_{0.95}Y_{0.05}FeO_3$ and **d** $Bi_{0.90}Y_{0.10}FeO_3$

spectra of first derivative of absorbance with wavelength ($dA/d\lambda$ versus λ plot) (Thota et al. 2009; Thota and Kumar 2009). The band gap of BYFO increases from 1.97 to 2.29 eV with increase in yttrium doping (as shown in Table 1) and such an increase in the band gap is also supported by the first-principle calculations (Zhang et al. 2010). This increase in band gap result an enhancement of photo catalytic activity in Y-doped BFO nanoparticle. The correlation between band gap and photo catalytic activity was also reported (Datta et al. 2008). The bumps around 350 nm may be due to the ligand to metal and metal to metal charge transfer. Our results clearly suggest that the band gap of $BiFeO_3$ can be tuned by yttrium doping to increase its operational range.

Photoluminescence (PL) spectra of all the samples are presented in Fig. 5. It shows several broad emissions within 550–700 nm, which is within the visible emission range. There is no observable change in peak positions due to doping. These intrinsic emissions are due to band to band transition of BFO and can be used to decompose organic contaminant easily.

The photo catalytic activity of BYFO was performed by the degradation of organic contaminant RhB in dark and

Table 1 Maxima of the first derivative and the band gap for different samples

Sample	Wavelength at $(dA/d\lambda)_{max}$ (nm)	Band gap (eV)
$BiFeO_3$	634.4	1.97
$Bi_{0.99}Y_{0.01}FeO_3$	587.0	2.13
$Bi_{0.95}Y_{0.05}FeO_3$	549.4	2.27
$Bi_{0.90}Y_{0.10}FeO_3$	545.6	2.29

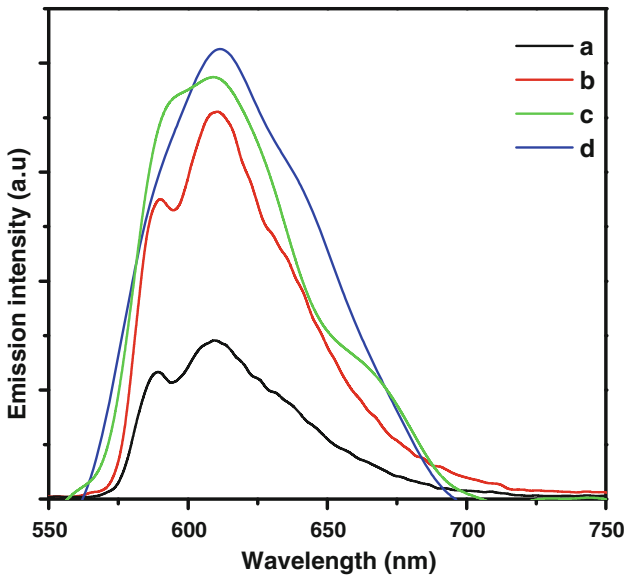

Fig. 5 PL spectra of **a** $BiFeO_3$, **b** $Bi_{0.99}Y_{0.01}FeO_3$, **c** $Bi_{0.95}Y_{0.05}FeO_3$ and **d** $Bi_{0.90}Y_{0.10}FeO_3$

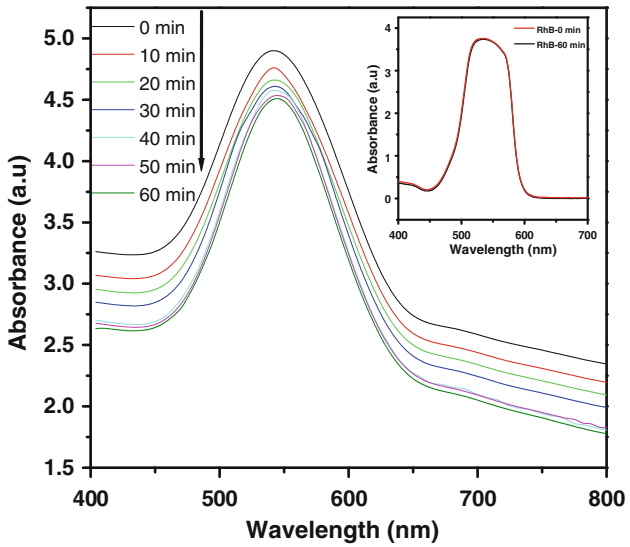

Fig. 6 Degradation of $Bi_{0.90}Y_{0.1}FeO_3$−Rhodamine-B system with time under illumination of 40 W lamp. *Inset* shows the zero degradation of pure Rhodamine-B with time under illumination of 40 W lamp

under visible light illumination of 40 W lamp. UV absorption curves showing the time dependent degradation of $Bi_{0.90}Y_{0.1}FeO_3$−RhB system is shown in Fig. 6. Self-degradation of RhB is almost zero when exposed to 40 W lamp for 1 h which is shown in the inset of Fig. 6, this may be due to absorption and desorption equilibrium. The degradation of RhB increased to 8 % when BYFO was added to it, which is due to photo catalysis together with sensitization. When the same solutions were kept in dark, there was no degradation of RhB as shown in Fig. 7.

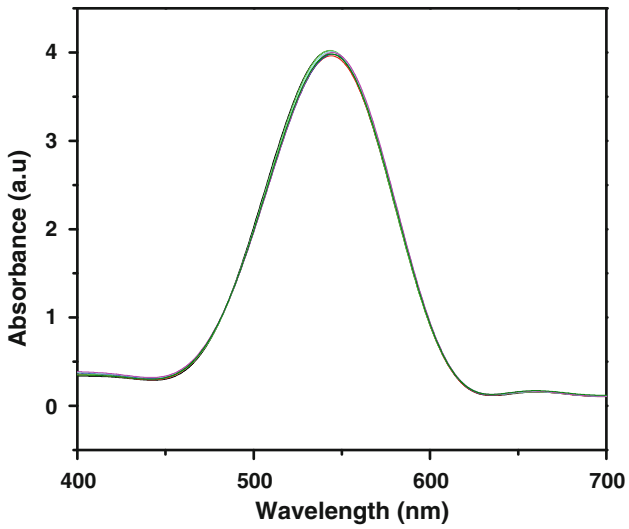

Fig. 7 Degradation of $Bi_{0.90}Y_{0.1}FeO_3$−Rhodamine-B system with time under dark

Conclusion

In summary, we have synthesized yttrium-doped bismuth ferrite nanoparticles by a modified Pechini method. Both XRD and TEM studies confirms the growth of pure BFO/BYFO in nanocrystalline form. FTIR spectra reveal the presence of various theoretically predicted peaks associated with the formation of BFO and BYFO. The band gap of the prepared BFO and BYFO nanoparticles varies from 1.97 to 2.29 eV, that is, within the visible range of the sunlight. This property of these nanoparticles can be utilized in photo catalytic decomposition of organic contaminants, such as RhB under visible light irradiation. We have explored and observed that RhB degrade up to 8 % while mixed with $Bi_{0.90}Y_{0.1}FeO_3$ for 1 h under 40 W lamp due to photo catalysis together with sensitization.

Acknowledgments The authors would like to acknowledge financial support from the Department of Science and Technology (DST), Govt. of India (Project no. SR/FTP/PS-66/2008). The authors also like to acknowledge the financial support from Board of Research in Nuclear Science (BRNS) (Project no. 2011/37P/14/BRNS), Department of Atomic Energy (DAE), Govt. of India.

References

Cheong SW, Mostovoy M (2007) Multiferroics: a magnetic twist for ferroelectricity. Nat Mater 6:13–20

Datta A, Priyam A, Bhattacharyya SN, Mukherjea KK, Saha A (2008) Temperature tunability of size in CdS nanoparticles and size

dependent photocatalytic degradation of nitroaromatics. J Colloid Interface Sci 322(1):128–135
Eerenstein W, Morrison FD, Dho J, Blamire MG, Scott JF, Mathur ND (2005) Comment on epitaxial $BiFeO_3$ multiferroic thin film heterostructures. Science 307(5713):1203a
Eerenstein W, Mathur ND, Scott JF (2006) Multiferroic and magnetoelectric materials. Nature 442:759–765
Fiebig M (2005) Revival of the magnetoelectric effect. J Phys D Appl Phys 38(8):R123
Gao F, Chen XY, Yin KB, Dong S, Ren ZF, Yuan F, Yu T, Zou ZG, Liu JM (2007) Visible-light photocatalytic properties of weak magnetic $BiFeO_3$ nanoparticles. Adv Mater 19(19):2889–2892
Li S, Condrate RA, Jang SD, Spriggs RM (1989) FTIR and Raman spectral study of the preparation of lead zirconate ($PbZrO_3$) by a solgel process in a non-flowing air atmosphere. J Mater Sci 24(11):3873–3877
Lee YH, Wu JM, Chueh YL, Chou LJ (2005) Low-temperature growth and interface characterization of $BiFeO_3$ thin films with reduced leakage current. Appl Phys Lett 87(17):172901–172903
Lou J, Maggard PA (2006) Hydrothermal synthesis and photocatalytic activities of $SrTiO_3$-coated Fe_2O_3 and $BiFeO_3$. Adv Mater 18(4):514–517
Lu XM, Xie JM, Song YZ, Lin JM (2007) Surfactant-assisted hydrothermal preparation of submicrometer-sized two-dimensional $BiFeO_3$ plates and their photocatalytic activity. J Mater Sci 42(16):6824–6827
Luo W, Zhu LH, Wang N, Tang HQ, Cao MJ, She YB (2010) Efficient removal of organic pollutants with magnetic nanoscaled$BiFeO_3$ as a reusable heterogeneous Fenton-like catalyst. Environ Sci Technol 44(5):1786–1791
Nakagawa I, Walter JL (1969) Optically active crystal vibrations of the alkali-metal nitrate. J Chem Phys 51(4):1389–1397
Pechini MP (1967) US Patent No. 3.330.697
Park T, Papaefthymiou G, Viescas A, Moodenbaugh A, Wong S (2007) Size-dependent magnetic properties of single-crystalline multiferroic $BiFeO_3$ nanoparticles. Nano Lett 7(3):766–772
Rao GVS, Rao CNR (1970) Infrared and electronic spectra of rare earth perovskites: ortho chromites, -manganites and -ferrites. Appl Spectrosc 24:436–445
Ramesh R, Spaldin NA (2007) Multiferroics: progress and prospects in thin films. Nat Mater 6:21–29
Roy SC, Sharma GL, Bhatnagar MC (2007) Large blue shift in the optical band-gap of sol–gel derived $Ba_{0.5}Sr_{0.5}TiO_3$ thin films. Solid State Commun 141(5):243−247
Som KK, Molla S, Bose K, Chaudhury BK (1992) Nonlinear physical properties of amorphous $Bi_4Sr_3Ca_3Cu_yO_x$ semiconducting oxides with y between 0 and 5. Phys Rev B 45(4):1655–1659
Slamovich EB, Aksay IA (1996) Structure evolution in hydrothermally processed (<100 C) $BaTiO_3$ films. J Am Ceram Soc 79(1):239–247
Singh SK, Ishiwara H (2006) Doping effect of rare-earth ions on electrical properties of $BiFeO_3$ thin films fabricated by chemical solution deposition. Jpn J Appl Phys 45:3194–3197
Thota S, Kumar J (2008) Sol-gel synthesis and behaviour of nickel containing ZnO nanoparticles. J Nanosci Nanotechnol 8(8): 4073−4080
Thota S, Kumar A, Kumar J (2009) Optical, electrical and magnetic properties of Co_3O_4 nanocrystallites obtained by thermal decomposition of sol-gel derived oxalates. Mater Sci Eng, B 164(1):30–37
Wang Y, Zhou L, Zhang M, Chen X, Liu J, Liu Z (2004) Room-temperature saturated ferroelectric polarization in $BiFeO_3$ ceramics synthesized by rapid liquid phase sintering. Appl Phys Lett 84(10):1731–1733
Wang J et al. (2005) Science response to comment on epitaxial $BiFeO_3$ multiferroic thin film heterostructures. 307(5713):1203b
Wang DH, Goh WC, Ning M, Ong CK (2006) Effect of Ba doping on magnetic, ferroelectric, and magnetoelectric properties in mutiferroic $BiFeO_3$ at room temperature. Appl Phys Lett 88(21): 212907–212909
Yuan GL, Or SW (2006) Multiferroicity in polarized single-phase $Bi_{0.875}Sm_{0.125}FeO_3$ ceramics. J Appl Phys 100(2):024109–024113
Zhang ST et al (2006) Substitution-induced phase transition and enhanced multiferroic properties of $Bi_{1-x}La_xFeO_3$ ceramics. Appl Phys Lett 88(16):162901–162903
Zhang ST, Pang LH, Zhang Y, Lu MH, Chen YF (2006) Preparation, structures, and multiferroic properties of single phase $Bi_{1-x}La_xFeO_3$ ($x = 0$–0.40) ceramics. J Appl Phys 100(11):114108
Zhang Z, Wu P, Chen L, Wang JL (2010) Systematic variations in structural and electronic properties of $BiFeO_3$ by A-site substitution. Appl Phys Lett 96(1):012905–012907